

## *Supplementary Information*

# Nanostructured manganese oxides as highly active catalysts for enhanced hydrolysis of bis(4-nitrophenyl)phosphate and catalytic decomposition of methanol

Martin Štastný<sup>\*1,2</sup>, Gloria Issa<sup>3</sup>, Daniela Popelková<sup>1</sup>, Jakub Ederer<sup>2</sup>, Martin Kormunda<sup>4</sup>, Sylvie Kříženecká<sup>2</sup>, and Jiří Henych<sup>1,2</sup>

<sup>1</sup>Institute of Inorganic Chemistry of the Czech Academy of Sciences, 250 68, Řež, Czech Republic

<sup>2</sup>Faculty of Environment, University of Jan Evangelista Purkyně in Ústí nad Labem, Pasteurova 3632/15, 400 96 Ústí nad Labem, Czech Republic

<sup>3</sup>Institute of Organic Chemistry with Centre of Phytochemistry, Bulgarian Academy of Sciences, Ak. G. Bontchev str., bl.9, Sofia, 1113, Bulgaria

<sup>4</sup>Faculty of Science, University of Jan Evangelista Purkyně in Ústí nad Labem, Pasteurova 3632/15, 400 96 Ústí nad Labem, Czech Republic

[stastny@iic.cas.cz](mailto:stastny@iic.cas.cz)

## S1. Characterization methods

Powder X-ray diffraction (XRD) patterns were obtained using Bruker D2 diffractometer equipped with a conventional X-ray tube (Cu K $\alpha$  radiation, 30 kV, 10 mA) and LYNXEYE 1-dimensional detector. The primary divergence slit module width 0.6 mm, Soler Module 2.5, Airscatter screen module 2 mm, Ni Kbeta-filter 0.5 mm, step 0.00405°, and time per step 0.3 s were used. The qualitative analysis was performed with a DiffracPlus Eva software package (Bruker AXS, Germany) using a JCPDS PDF-2 database. The crystallographic information file (CIF) was obtained from the Crystallography Open Database (COD) <sup>1</sup>. The polyhedral crystal structures of manganese catalysts were made by using Vesta software, version 3.4.8 <sup>2</sup>.

The crystallite sizes were calculated from diffraction line broadening using the *Scherrer formula* <sup>3</sup>:

$$a = \frac{K\lambda}{\beta \cos \theta} \quad (1)$$

where  $K$  is the shape factor,  $\lambda$  is the wavelength of the applied radiation,  $\beta$  is the broadening of the diffraction line, and  $\theta$  is the diffraction angle.

The specific surface area and porosity of the powder samples were measured using a Quantachrome NOVA 4200e instrument at liquid nitrogen temperature. The samples were degassed for 6 hours at 120 °C. The Brunauer–Emmett–Teller (BET) method was used for surface area calculation. *The BJH method* (Barrett, Joyner, and Halenda) was used for calculating pore size distributions <sup>4</sup>. The morphology of the samples was measured on an FEI Talos F200X transmission electron microscope. Raman investigation was carried out on a DXR Raman microscope (Thermo Fischer Scientific, Inc., Waltham, MA) equipped with a 532 nm laser.

The TPR/TG (temperature-programmed reduction/ thermogravimetric) analyses were performed in a Setaram TG92 instrument. Typically, 40 mg of the sample was placed in a microbalance crucible and heated in a flow of 50 vol. % H<sub>2</sub> in Ar (100 cm<sup>3</sup>min<sup>-1</sup>) up to 773 K at 5 Kmin<sup>-1</sup> and a final hold-up of 1 h.

X-ray photoelectron spectroscopy (XPS) measurements were performed using a SPECS PHOIBOS 100 hemispherical analyzer with a 5-channel detector and a SPECS XR50 X-ray source equipped with an Al/Mg anodes. Survey spectra were recorded with a pass energy of 40 eV, and the high-resolution spectra were recorded as a sum of 5 acquisitions with a pass energy of 10 eV. A Shirley background profile was used for data processing in CasaXPS software. The charge compensation was made by a C 1s peak calibration process. The C 1s peaks have a single peak character attributed to C–C bonds and calibrated to the binding energy (BE) of 284.8 eV.

Elemental analyses were performed using desktop X-ray fluorescence spectroscopy (XRF) using an Epsilon 3X instrument (PANalytical, the Netherlands) with an X-ray tube (Ag cathode, up to 50 kV) and a Peltier-cooled large-area Si-drift detector (SDD). Micro-milled samples were analyzed as a powder in nylon cells with Mylar foil bottoms. The intensities of the analytical signal were optimized for selected element K and calibrated using certified reference materials.

Acid-base potentiometric titrations were performed on an automatic titrator controlled by a PC (794 Basic Titrino, Metrohm, Switzerland) with a potentiometric endpoint determination. Typically, 75 mg of sample catalyst was weighed into the titration vessel, 30 mL of NaCl ( $0.1 \text{ mol}\cdot\text{dm}^{-3}$ ), 3 ml of a standardized solution of HCl ( $0.1 \text{ mol}\cdot\text{dm}^{-3}$  in  $0.1 \text{ mol}\cdot\text{dm}^{-3}$  NaCl) were added, and the suspension was mixed and bubbled by nitrogen for 30 minutes. Subsequently, the samples were titrated with standardized  $0.1 \text{ mol}\cdot\text{dm}^{-3}$  NaOH (in  $0.1 \text{ mol}\cdot\text{dm}^{-3}$  NaCl) with continuous stirring with a magnetic bar under a nitrogen atmosphere. The rate of titrant was  $0.1 \text{ ml}\cdot\text{min}^{-1}$  in 0.05 ml aliquots.

To monitor and identify BNPP and its degradation products were used two HPLC systems: a) HPLC with a diode array detector (DAD) Dionex UltiMate 3000 (Thermo Scientific <sup>TM</sup>, Palo Alto, USA). Chromatographic analysis was carried out in a reverse phase system (RPLC-C18) on the Accucore<sup>TM</sup> column,  $2.6 \mu\text{m}$ , PFP,  $150 \times 4.6\text{mm}$ . For gradient elution, mobile phase acetonitrile (ACN)/water ( $\text{H}_2\text{O}$ ) acidified with formic acid (HCOOH, 0.1%) was used. The gradient was set as follows: -1.0 min  $\rightarrow$  0 min: Column equilibration (30% ACN-HCOOH (0.1%) / 70%  $\text{H}_2\text{O}$ -HCOOH (0.1%); 0 min  $\rightarrow$  5 min: 30%

ACN-HCOOH (0.1%) / 70% H<sub>2</sub>O-HCOOH (0.1%) → 60% ACN-HCOOH (0.1%)/40% H<sub>2</sub>O-HCOOH (0.1%); 5 min → 6 min: 60% ACN-HCOOH (0.1%) /40% H<sub>2</sub>O-HCOOH (0.1%) → 95% ACN-HCOOH (0.1%)/5% H<sub>2</sub>O-HCOOH (0.1%). The flow rate of the mobile phase was set to 1.0 ml·min<sup>-1</sup> in the entire gradient, 30° C column temperature, and 15 µl volume injection. Data were collected at the absorption maximum of the individual substances. Wavelengths corresponding to 280 nm for BNPP and 320 nm 4-NP were set on the DAD detector. Data collection and evaluation was performed using the Chromeleon Chromatography Data System (CDS) software (Thermo Scientific);

b) HPLC system coupled with mass spectrometry (HPLC-MS) Infinity II (Agilent Technologies, USA) using the same chromatographic column heated at 30°C. Chromatographic separation was achieved using a binary mobile phase (water (A)/acetonitrile (B)) with 0.1% CH<sub>3</sub>COOH delivered in the gradient mode at a flow rate of 1.0 ml·min<sup>-1</sup>. Gradient elution started at 60% of B (0–5 min) and linearly increased to 95% of B 0.1 min; then maintained at 95% of B for 50 sec (5.1 – 6 min); then decreased to 60% of B (6–8 min) for re-equilibration of the column. The injection volume of the samples was 2 µl. Analytes quantification was performed with a mass spectrometer 6495 with triple quadrupole (Agilent Technologies, USA). Mass spectrometric detection was performed using an MS2 scan with an electrospray ionization (ESI) source in negative mode. The conditions were gas temperature 150°C; gas flow 12 L·min<sup>-1</sup>; ion spray voltage 3500 V; sheat gas temperature 350°C; sheat gas flow 11 L·min<sup>-1</sup>; nebulizer 35 psi; nozzle voltage 300 V. Simultaneously, blank experiments were performed using the same procedure but without a powder catalyst. The amount of 4-nitrophenol (4-NP) produced by the catalytic reaction was expressed by its twice equimolar concentration (1:2) relative to the starting BNPP (assuming the release of two 4-NP molecules during the catalytic process).

Time-resolved absorption spectra were measured on a Perkin Elmer UV-Vis spectrophotometer, LAMBDA 35 (PerkinElmer Inc., USA), with UV WinLab software. Supernatants were measured against pure TRIS buffer (pH=7) as a reference. The whole spectrum was measured in the wavelength range from 200 to 800 nm.

### S1.1. X-ray powder diffraction (XRD)

The XRD patterns of as-prepared samples are presented in **Figure S1**.

How can be seen, all the diffraction peaks of sample denoted  $MnO\_1$  can be indexed to two polymorphs: Hexagonal akhtenskite;  $\epsilon$ - $MnO_2$  (JCPDS card No. 01-089-5171; space group: P63/mmc) and orthorhombic ramsdellite;  $\gamma$ - $MnO_2$  (JCPDS card No. 00-044-0142; point Group: 2/m 2/m 2/m), which are the product of  $KMnO_4$  and  $Mn(NO_3)_2$  in the reaction system<sup>5,6</sup>. The XRD patterns were characterized by broad and low-intensity peaks, indicating poor crystallinity. Akhtenskite has a hexagonal close packing structure with flakiness and plating, usually with the space group of P63/mmc. Synthetic akhtenskite may be used for supercapacitor applications<sup>7</sup>, or as an adsorbent for methylene blue removal<sup>8</sup>. Moreover, the XRD pattern of  $MnO\_1$  sample reveals a ramsdellite phase with an orthorhombic unit cell. The XRD pattern of sample  $MnO\_1$  was the same as the manganese oxides synthesized by Rossouw *et al.* (1992)<sup>9</sup>. On the contrary, the diffraction peaks of sample denoted  $MnO\_2$  were characterized by the sharp and narrow peaks indicate the higher crystallinity, which corresponds to a typical cryptomelane-like  $\alpha$ - $MnO_2$  pattern having a tetragonal crystal structure with I4/m space group (JCPDS card No. 00-004-0603)<sup>10</sup>. The XRD pattern of as-prepared sample  $MnO\_3$  showed the characteristic peaks at  $2\theta = 12^\circ, 24.7^\circ, 36.7^\circ,$  and  $66.1^\circ$  assigning to the hexagonal birnessite-type manganese oxide  $\delta$ - $MnO_2$  (Birnessite-K, syn –  $(K)_xMnO_2 \cdot H_2O$ , JCPDS card No. 00-018-0802; P63/mmc space group). The broadened diffraction peaks with low intensity indicate the typical characteristic of nano-crystalline<sup>11</sup>. The reaction of an aqueous solution of  $Mn(NO_3)_2$  and ammonia solution ( $MnO\_4$ ) leads to tetragonal hausmannite-type manganese oxide (JCPDS card No. 01-089-4837; body-centered I41/amd space group) of  $Mn_3O_4$ <sup>12</sup>.

The phase composition, unit cell parameters, and crystallite size for prepared manganese-based catalysts are presented in **Table S1**. On the contrary, the diffraction peaks of sample  $Mn_xO_y-HT$ , synthesized by using a template method, were characterized with sharp and intensive diffraction reflections at  $2\theta$   $23.1^\circ, 33.1^\circ, 38.2^\circ, 55.2^\circ,$  and  $65.9^\circ$ , corresponding to  $Mn_2O_3$  phase (JCPDS card No. 24-0508) with relatively large crystallites (see **Table S1**). The characteristic diffraction peaks of  $Mn_5O_8$  (JCPDS card No. 00-039-

1218) were apparent at about 36.1°, 37.5°, and 65.2°. The appearance of additional reflections at about 18.1° corresponds to the  $Mn_3O_4$  phase (JCPDS card No. 24-0734) with a tetragonal structure with good crystallinity (about 10 %) were registered.

Based on the XRD results, the polyhedral crystal structures of manganese catalysts were made using Vesta software, as shown in **Figure S2**.

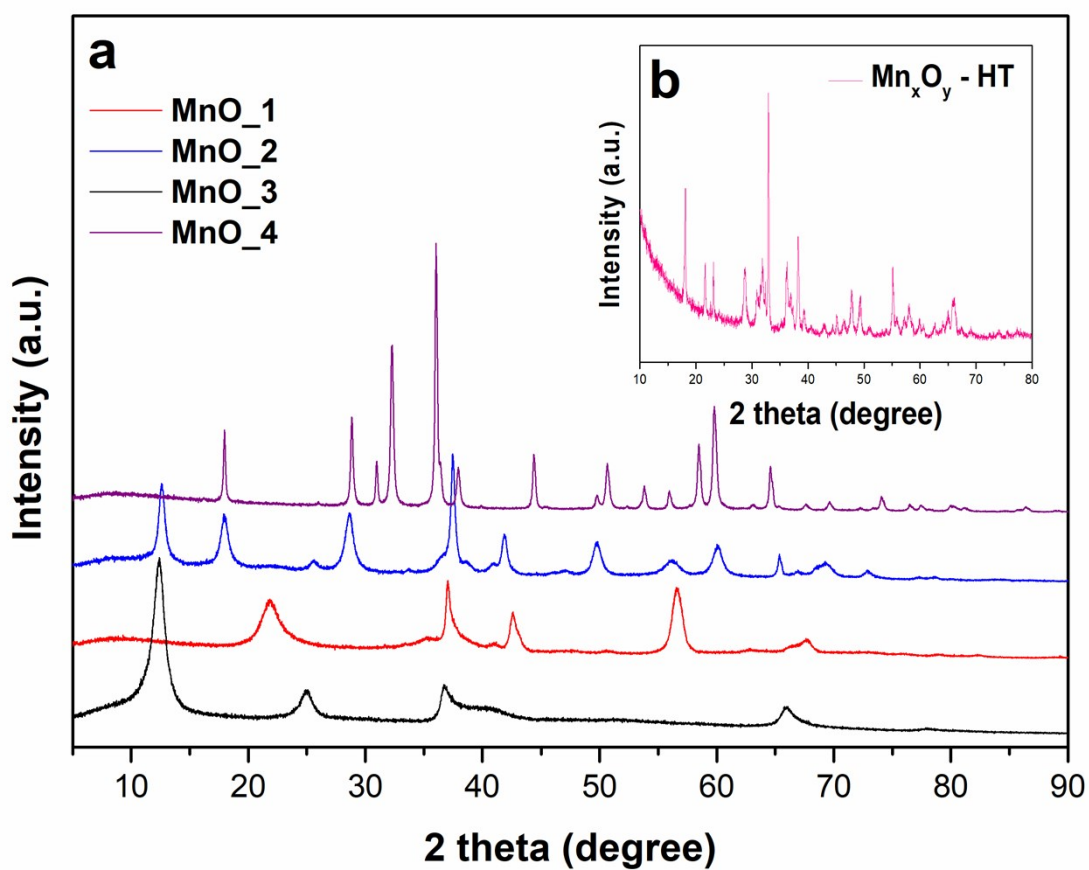
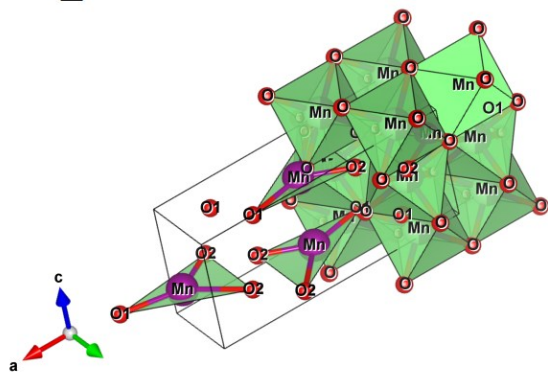


**Fig. S1.** XRD patterns of  $MnO_x$  samples.

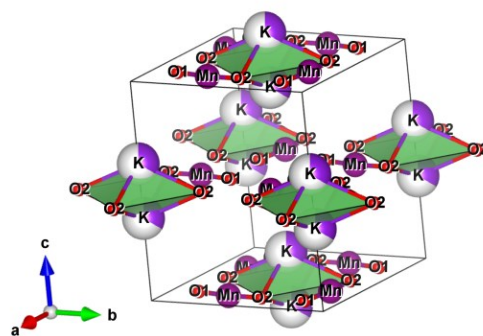
**Table S1.** The phase composition, unit cell parameters, space group, and crystallite size for manganese oxides-based catalysts.

Sample	The phase composition, space group	Unit cell parameters, x10 nm	Crystallite size, nm
<b>MnO_1</b>	Ramsdellite, syn MnO <sub>2</sub>	A = 9.542	6 nm
	Orthorhombic Pbnm	B = 2.765	
	Akhtenskite, syn MnO <sub>2</sub>	C = 4.379	
	Hexagonal P63/mmc	A = 2.762 C = 4.389	15 nm
<b>MnO_2</b>	Cryptomelane K(Na)Mn <sub>8</sub> O <sub>16</sub>	A = 9.808	18 nm
	Tetragonal I4/m	B = 2.870	
		C = 9.983	
<b>MnO_3</b>	Birnessite-K, syn – (K) <sub>x</sub> MnO <sub>2</sub> .H <sub>2</sub> O	A = 2.818	7 nm
	Hexagonal P63/mmc	C = 14.273	
<b>MnO_4</b>	Hausmannite Mn <sub>3</sub> O <sub>4</sub>	A = 5.765	49 nm
	Tetragonal – Body-centered I41/amd	C = 9.471	
<b>Mn<sub>x</sub>O<sub>y</sub>-HT</b>	24 % Mn <sub>2</sub> O <sub>3</sub> (cubic Ia-3)	A = B = C = 9.411	85 nm
	67 % Mn <sub>5</sub> O <sub>8</sub> (monoclinic C2/m)	A = B = 5.974	33 nm
	9% Mn <sub>3</sub> O <sub>4</sub> (tetragonal I41/amd)	C = 4.895	66 nm
		A = 5.870	
		B = 6.340	
		C = 5.870	

MnO\_1

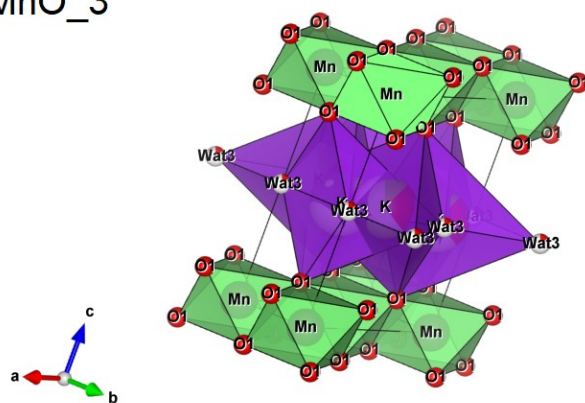


MnO\_2

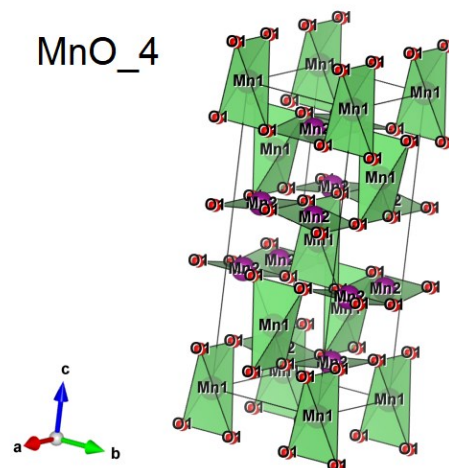


[MnO<sub>6</sub>] octahedra

MnO\_3



MnO\_4



MnxOy-HT

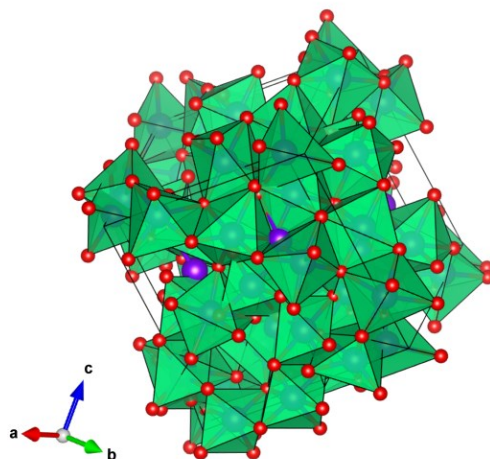


Fig. S2. The polyhedral structures of MnO<sub>x</sub> samples.

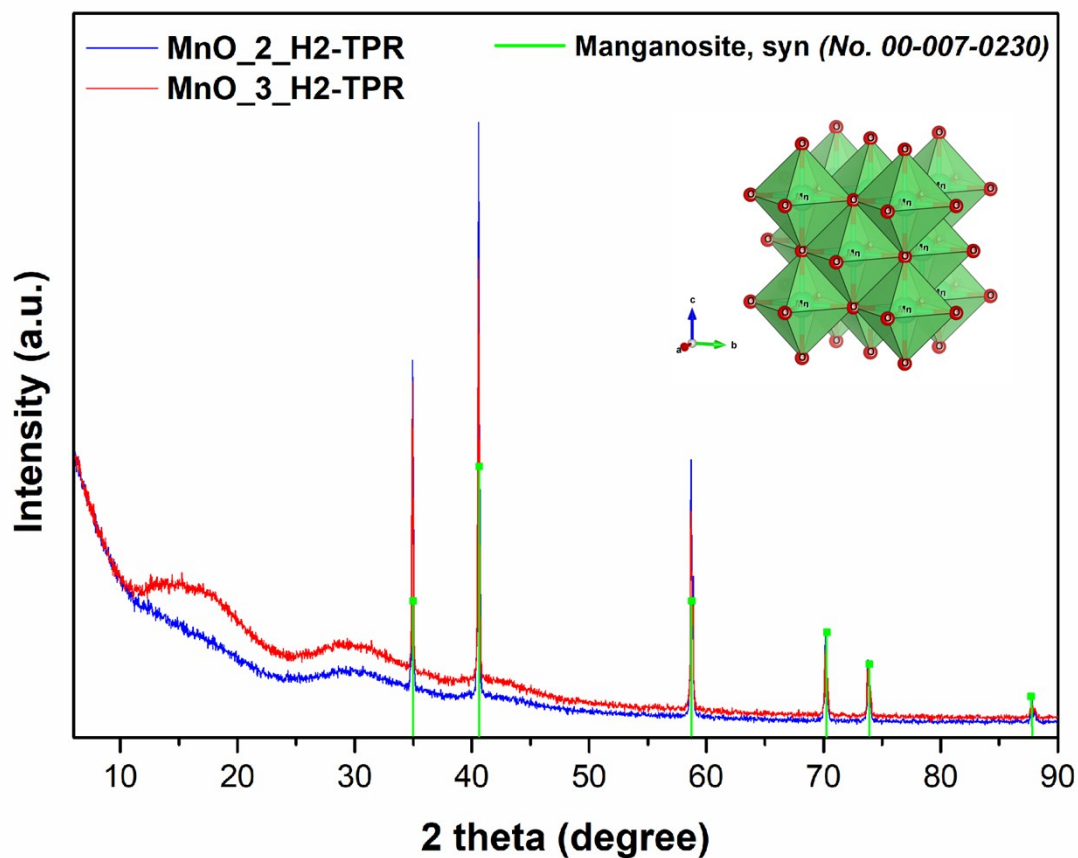


Fig. S3. XRD patterns of  $\text{MnO}_x$  obtained after  $\text{H}_2$ -TPR.

Table S2. The phase composition, unit cell parameters, space group, and crystallite size for manganese catalysts obtained after  $\text{H}_2$ -TPR.

Sample	The phase composition, space group	Unit cell parameters, x10 nm	Crystallite size, nm
<b>MnO_2_H2-TPR</b>	Manganosite, syn MnO Cubic; face-centered Fm-3m	A = B = C = 4.445	142 nm
<b>MnO_3_H2-TPR</b>	Manganosite, syn MnO Cubic; face-centered Fm-3m	A = B = C = 4.445	135 nm

## S1.2. Raman investigations

According to XRD (see **Fig. S1**), the only sample labeled as *MnO\_1* contains akhtenskite and ramsdellite, whereas samples denoted as *MnO\_2*, *MnO\_3*, *MnO\_4*, and *Mn<sub>x</sub>O<sub>y</sub>-HT* are composed of cryptomelane, birnessite, haussmanite, and multi-phase  $Mn_xO_y$  (cubic  $Mn_2O_3$ , monoclinic  $Mn_5O_8$ , and tetragonal  $Mn_3O_4$ ), respectively (see **Table S1**).

Raman spectroscopy was used as a complementary tool to XRD for the analysis of phase composition and structure of as-prepared manganese oxide materials.

**Figure S4** shows the Raman spectra collected at room temperature of manganese oxide samples prepared by different synthetic procedures using different precursors.

The Raman spectrum of *MnO\_1* sample exhibits several weak and strong bands (165, 221, 257, 296, 379, 472, 492, 528, 572, 613, and 643  $cm^{-1}$ ). Their position corresponds with the results of the analysis of manganese oxide materials with different content of ramsdellite (*R*- $MnO_2$ ) and akhtenskite ( $\epsilon$ - $MnO_2$ )<sup>13,14</sup>. The two sharp peaks at 613 and 643  $cm^{-1}$  can be attributed to the stretching mode of the Mn–O bond in  $[MnO_6]$  octahedra<sup>15</sup>. It should be emphasized that the less intense band at 572  $cm^{-1}$  belongs to ramsdellite *R*- $MnO_2$ .

For the cryptomelane-type  $\alpha$ - $MnO_2$  (sample *MnO\_2*), weak RS bands located at 176, 381, 477, 568, and 635  $cm^{-1}$  are characteristic  $\alpha$ - $MnO_2$  phase<sup>16</sup>. The peak situated at 635  $cm^{-1}$  might be related to Mn–O vibrations perpendicular to the direction of the  $[MnO_6]$  octahedral double chains<sup>17</sup>. Moreover, the weak bands at 381 and 176  $cm^{-1}$  match well with the tetragonal unit cell (space group  $I4/m$ )<sup>15</sup>.

Sample *MnO\_3*, which is composed of pure birnessitic phase, shows two characteristic peaks centered at 564 and 648  $cm^{-1}$ , confirm the birnessite-type  $MnO_2$ . The Raman band at 648  $cm^{-1}$  can be viewed as the symmetric stretching vibration (Mn–O) of the  $MnO_6$  groups, and the band at 564  $cm^{-1}$  is attributed to the (Mn–O) stretching vibration in the basal plane of  $MnO_6$  sheets. On the other hand, the less intense RS bands at 616 and 637  $cm^{-1}$  might reflect the content of  $Mn^{3+}$  in  $Mn^{3+}$ -rich rows typical for hexagonal birnessite, which is consistent with the XPS results (see **Figure S7c**)<sup>18,19</sup>.

As can be further seen, in the case of a sample *MnO\_4*, three peaks at 312, 365, and 650  $\text{cm}^{-1}$  were observed and could be assigned to the presence of the pure hausmannite. The obtained results fully correspond with the Raman database (dashed line), XRD results, and the literature <sup>20,21</sup>.

The multi-phase *Mn<sub>x</sub>O<sub>y</sub>-HT* sample shows several RS bands at 175, 221, 262, 480, 535, 583, 625, and 653  $\text{cm}^{-1}$ . The less intense bands at 480, 535, 583, and 625  $\text{cm}^{-1}$  confirm the binary layered structure of  $\text{Mn}_5\text{O}_8$  <sup>22</sup>. The Raman spectrum is characterized by a very sharp peak at 653  $\text{cm}^{-1}$ , which was found on mineral Hausmannite ( $\text{Mn}_3\text{O}_4$ ) <sup>23</sup>, as well as in the bulk of  $\text{Mn}_2\text{O}_3$  <sup>24</sup>.

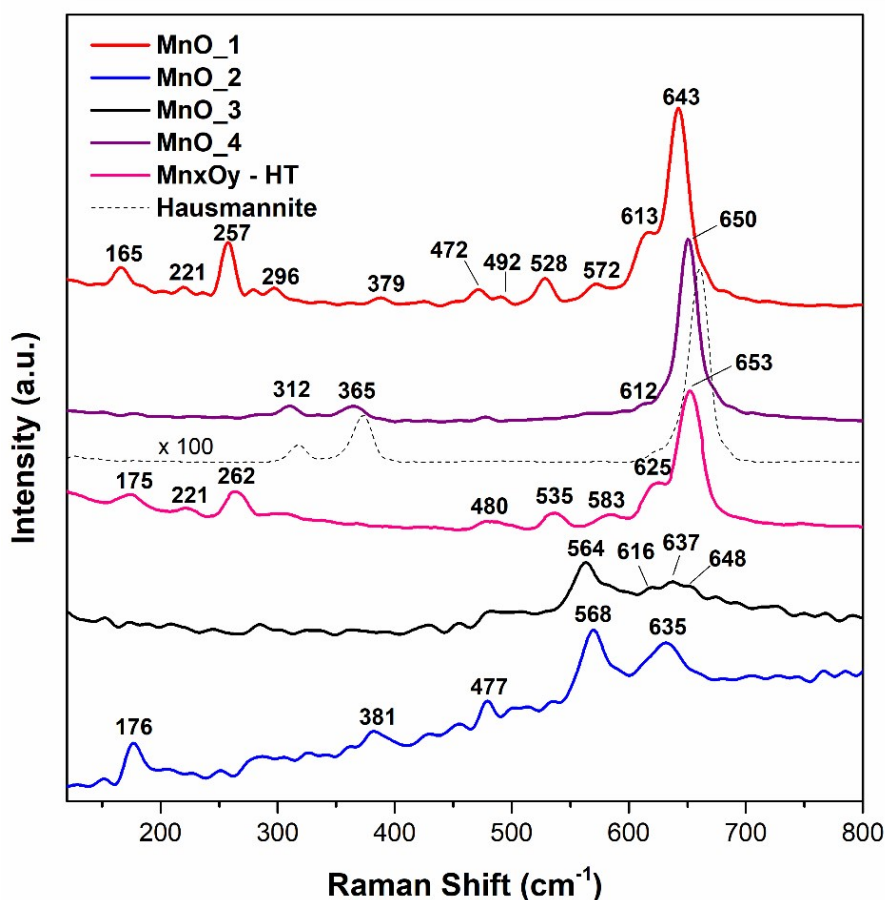


**Fig. S4.** Raman spectra of various manganese oxide catalysts.

### S.1.3. Temperature-programmed reduction with hydrogen

The profiles of ( $H_2$ -TPR) are presented in **Fig. S5**. The redox behavior of the materials is fully consistent with XRD and XPS results. The reduction of the manganese oxides can be described as follows:  $MnO_2 \rightarrow Mn_2O_3 \rightarrow Mn_3O_4 \rightarrow MnO$  <sup>25,26</sup>. As shown in **Fig. S5**, each  $H_2$ -TPR profile of the manganese oxide catalyst shows one or two main peaks attributed to the reduction of the manganese species. In general, the peaks in the temperature range from 543 K to 643 K can be assigned to the step-wise reduction of  $MnO_2$  to  $Mn_2O_3$  or  $Mn_2O_3$  to  $Mn_3O_4$ , and the peaks in the temperature range of 643 to 733 K can be assigned to the reduction of  $Mn_3O_4$  to  $MnO$  <sup>27</sup>. The TPR patterns of *MnO\_1*, *MnO\_4*, and *Mn<sub>x</sub>O<sub>y</sub>-HT* samples are similar and correspond to the reduction of  $MnO_2 \rightarrow Mn_2O_3 \rightarrow Mn_3O_4 \rightarrow MnO$ .

On the other hand, on sample *MnO\_2* and *MnO\_3* was observed reduction effect and significant shift of the profiles to lower temperatures compared to their analogs. In accordance with the XRD data and spectral measurements, this could be associated with the elimination of more labile lattice oxygen ion, shared with manganese. Besides, the XPS study clearly demonstrated the presence of a significant amount of  $Mn^{3+}$ ,  $Mn^{2+}$ , and oxygen defects in these samples, probably due to more Lewis acidic sites. The reduction peaks of *MnO\_4* and *Mn<sub>x</sub>O<sub>y</sub>-HT* are shifted to high temperature, which could be indexed as the pure intermediate  $Mn_5O_8$  ( $MnO_2 \cdot 2Mn_2O_3$ ) phase by XRD characterization <sup>28,29</sup>, probably due to the crystalline nature of the materials and the increasing particle size (see **Table S1**). This observation, combined with an increase in the ratio of the low temperature to high-temperature reduction effects, could indicate the increased  $Mn^{4+}$  content at the expense of manganese ions of lower oxidation state in the samples, and this result is in accordance with XPS results. In accordance with the XRD data, this could be provoked by the stabilization of  $Mn^{4+}$  ions <sup>30</sup>. On the other hand, the reduction of the *Mn<sub>x</sub>O<sub>y</sub>-HT* sample seems to be hindered as the first effect is much smaller and not well defined, and this is probably due to two reasons: i) in accordance with XRD data, the presence of  $Mn_3O_4$  phase (10%) and ii) in accordance with XPS data, presence of manganese ions in lower oxidation state ( $Mn^{2+}$ ) most probably formed during

the hydrothermal treatment in comparison with the other materials. This observation is also consistent with previous reports <sup>31</sup>.

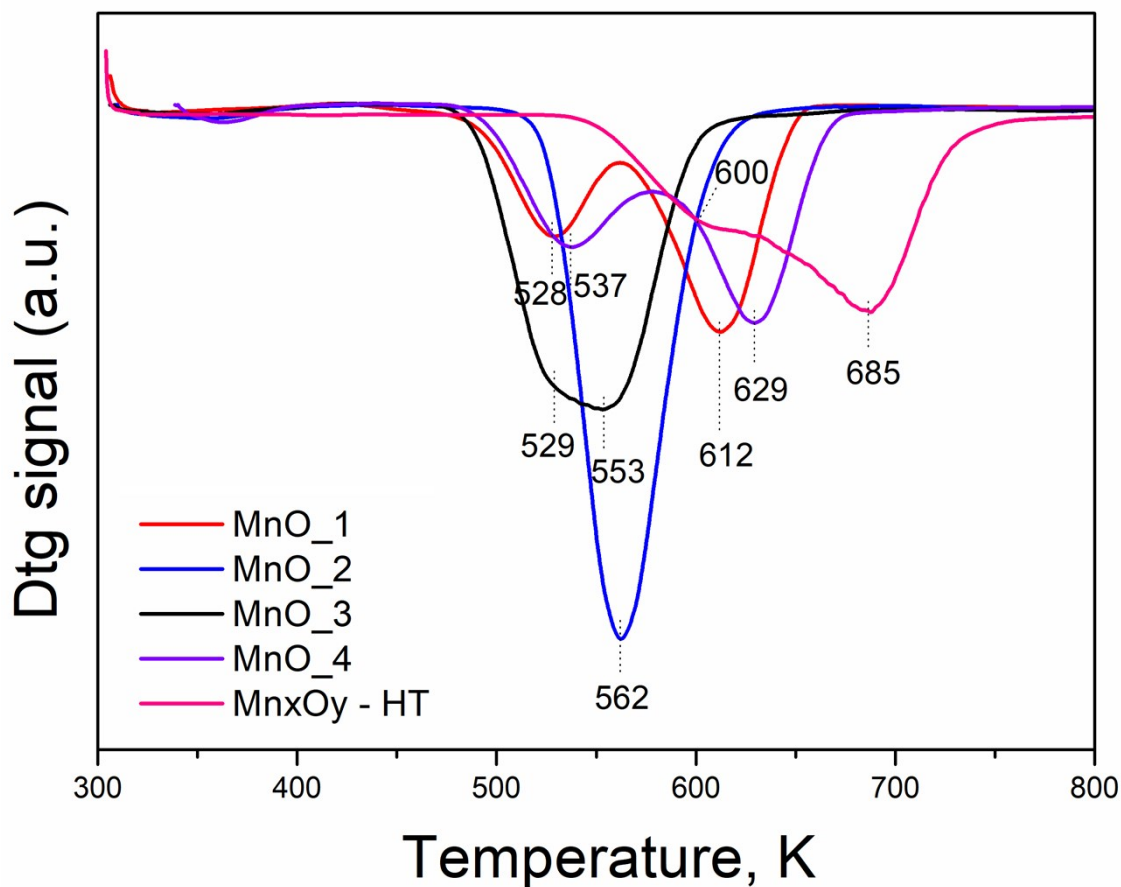


**Fig. S5.** H<sub>2</sub>-TPR profiles of the manganese oxide catalysts.

#### S1.4. BJH and BET

Nitrogen adsorption/desorption measurements confirmed the textural properties.

As shown in **Figure S6** (the Barrett–Joyner–Halenda (BJH) pore-size distribution plot and nitrogen adsorption/desorption isotherms), all manganese samples show the typical IUPAC type H3 hysteresis loop, suggesting the existence of mesopores. Type H3 is usually obtained with adsorbents having slit-shaped pores or the aggregates of other plate-like particles. Hysteresis loops are observed in the relative pressure range of 0.6–0.8 (not shown), which suggests the existence of mesopores filled up in this

pressure range. The BET specific surface area, pore-volume, and average pore size data were summarized in **Table S2**. As can be seen from **Table S2**, the samples generally exhibit relatively low specific surface areas (~ 24 - 62 m<sup>2</sup>/g) and low pore volumes (0.01–0.07 cc/g). The *MnO\_2* and *MnO\_3* samples exhibit a larger surface area and pore volume than *MnO\_1*, *MnO\_4*, and *Mn<sub>x</sub>O<sub>y</sub>-HT* samples.

The pure manganese oxides show low specific surface areas (<10 m<sup>2</sup>/g) and low pore volumes (0.02–0.03 cc/g).

**Table S3.** Summary of the nitrogen adsorption/desorption measurements and surface elemental compositions of the MnO<sub>x</sub> samples from Mn 2p<sub>3/2</sub> and O 1s XPS spectra.

Sample	Surface area (m <sup>2</sup> ·g <sup>-1</sup> )	Pore volume (cm <sup>3</sup> ·g <sup>-1</sup> )	Average pore size (nm)	Mn <sup>4+</sup> :Mn <sup>3+</sup> :Mn <sup>2+</sup>	O <sub>α</sub> /(O <sub>α</sub> + O <sub>β</sub> ) (%)
MnO_1	44	0.01	27.2	0:80:20	51
MnO_2	62	0.01	8.8	66:30:5	75
MnO_3	53	0.02	7.6	23:64:14	68
MnO_4	24	0.07	8.6	45:23:32	76
Mn <sub>x</sub> O <sub>y</sub> -HT	7.4	0.03	8.8	49:24:27	79

**Table S4.** Bulk and surface atomic composition from XRF and XPS analyses for different synthesized MnO<sub>x</sub> catalysts.

Sample	XPS				XRF
	C [at.%] <sup>a</sup>	K [at.%] <sup>a</sup>	Mn [at.%] <sup>a</sup>	O [at.%] <sup>a</sup>	Bulk K [wt.%] <sup>b</sup>
	C 1s	K 2p	Mn 2p <sub>3/2</sub>	O 1s	
MnO_1	11.1%	0.0%	27.1%	61.9%	0.0%
MnO_2	16.9%	3.8%	21.8%	57.5%	3.6%
MnO_3	10.6%	3.8%	24.1%	61.4%	4.1%
MnO_4	14.7%	0.0%	27.1%	58.1%	0.0%
Mn <sub>x</sub> O <sub>y</sub> -HT	12.8%	0.0%	27.3%	58.2%	0.0%

<sup>a</sup> Determined by XPS. <sup>b</sup> Determined by XRF.

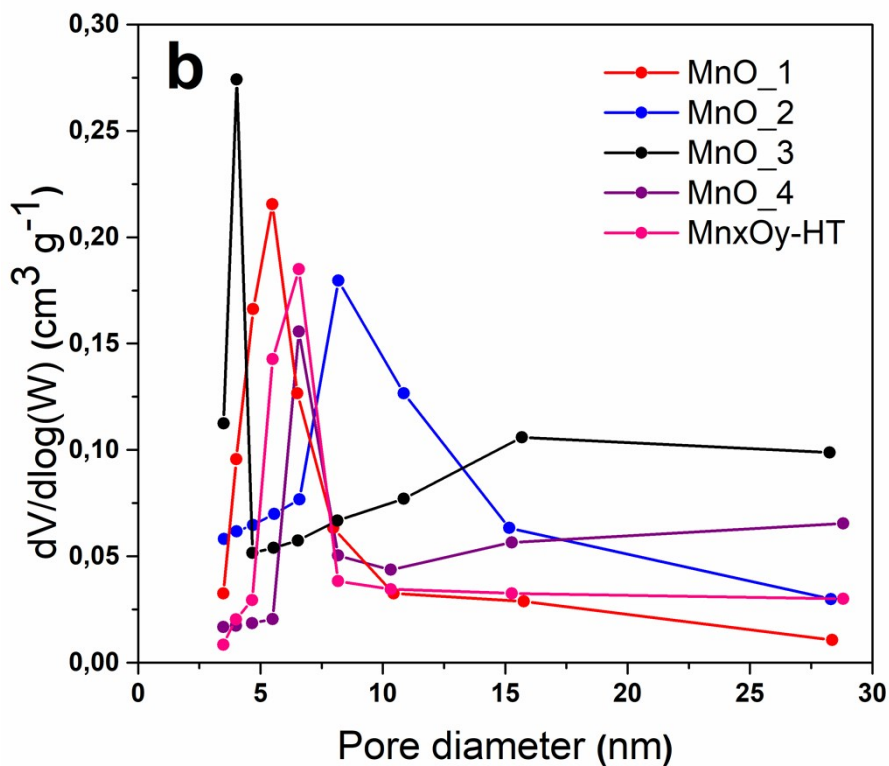
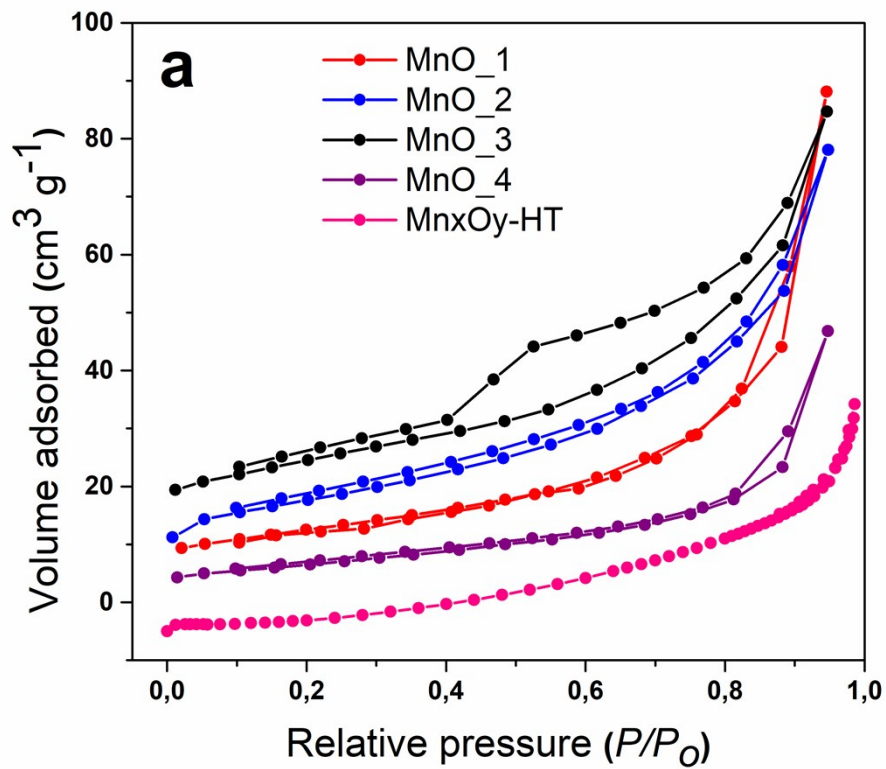


**Fig. S6.** Nitrogen adsorption/desorption isotherms (a) and pore-size distribution (b) of  $\text{MnO}_x$  samples.

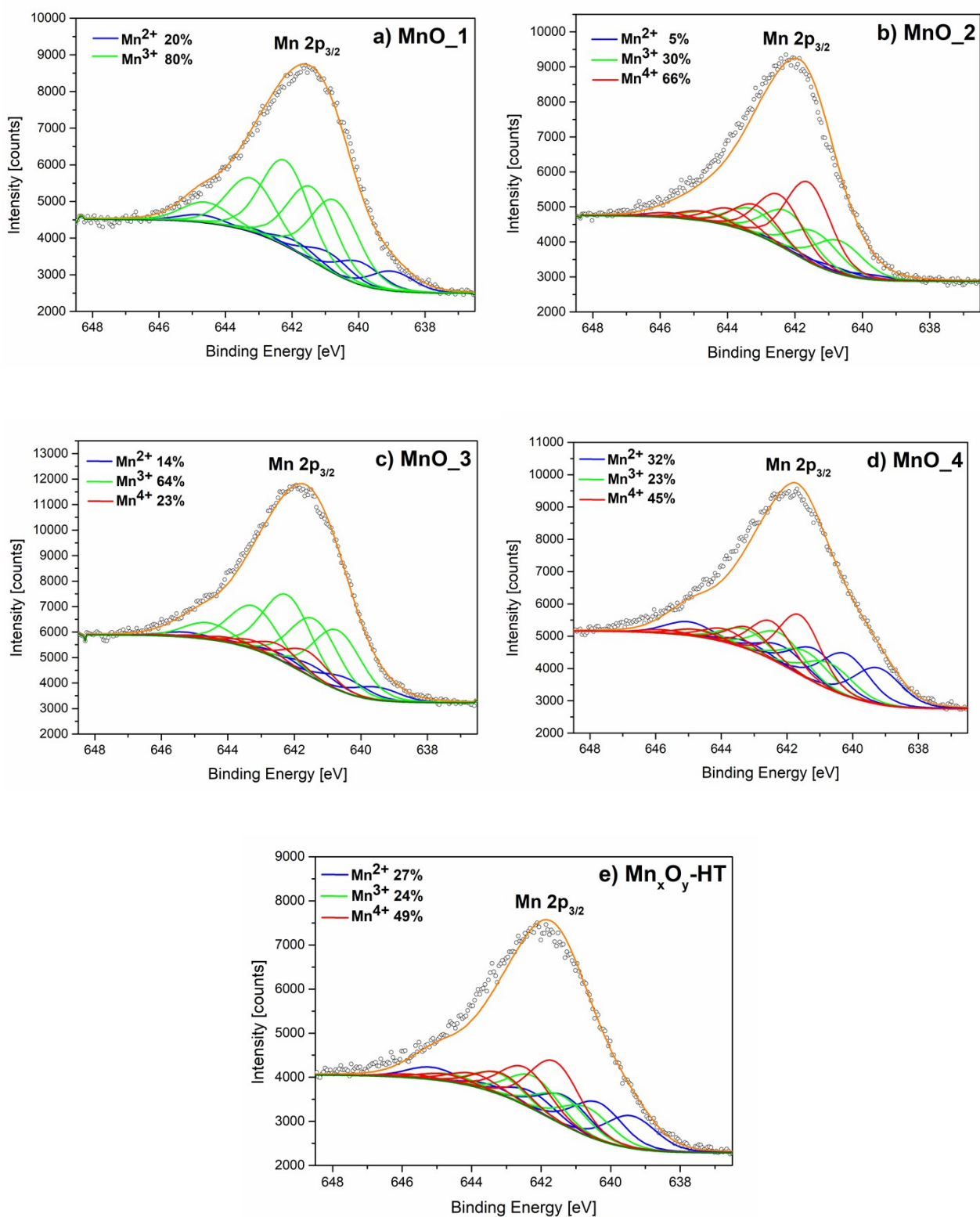


**Fig. S7.** Mn 2p<sub>3/2</sub> fitting spectra of MnO<sub>x</sub> catalysts prepared by different procedures. (a) MnO<sub>1</sub>; (b) MnO<sub>2</sub>; (c) MnO<sub>3</sub>; (d) MnO<sub>4</sub>, and (e) Mn<sub>x</sub>O<sub>y</sub>-HT.

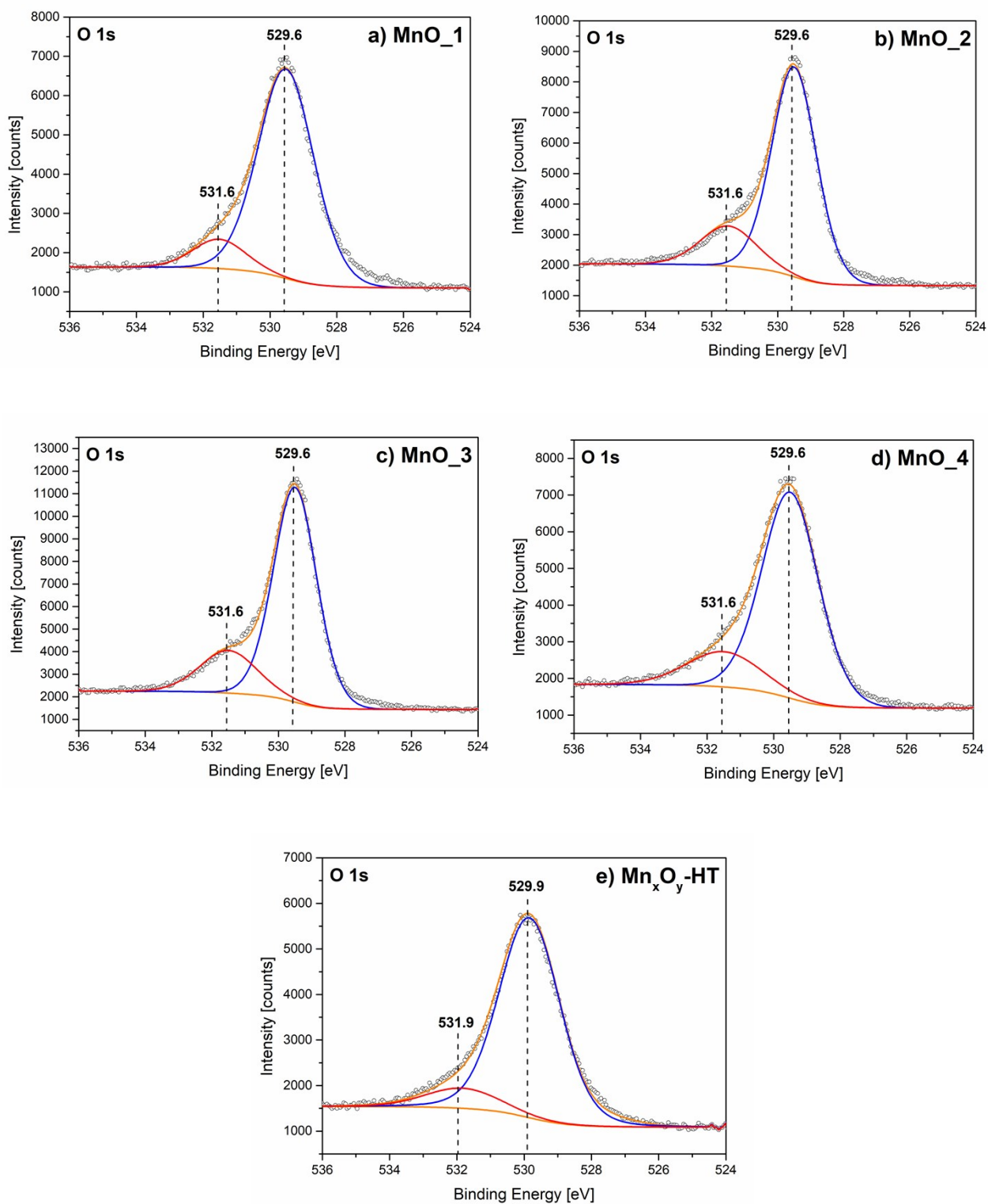


**Fig. S8.** O 1s XPS spectra of MnO<sub>x</sub> catalysts prepared by different procedures. (a) MnO<sub>1</sub>; (b) MnO<sub>2</sub>; (c) MnO<sub>3</sub>; (d) MnO<sub>4</sub>, and (e) Mn<sub>x</sub>O<sub>y</sub>-HT.

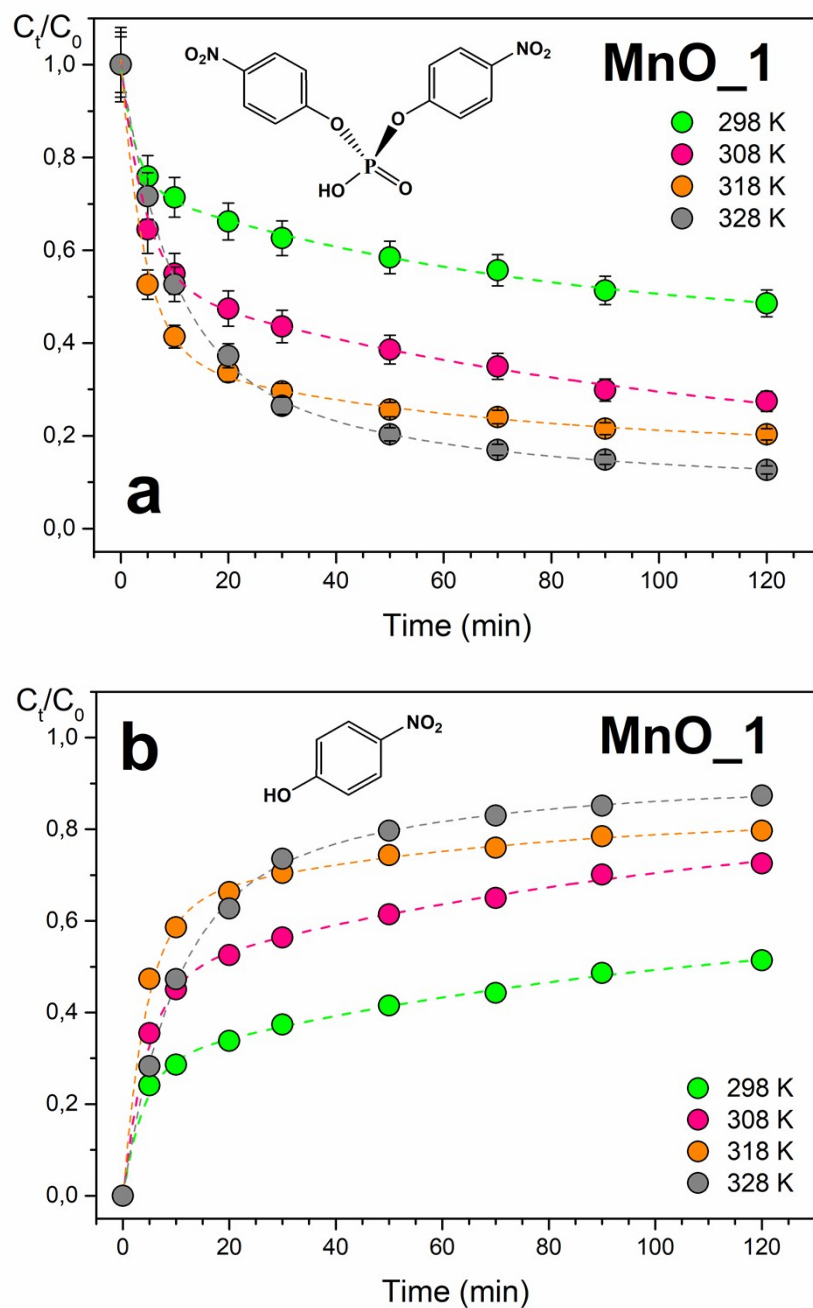


**Fig. S9.** Plots of pseudo-first-order kinetics of a) BNPP hydrolysis and b) 4-NP formation with 100 mg of MnO\_1 catalyst at various temperatures. Reaction conditions: pH=7.0, [BNPP]<sub>0</sub> = 50 mg·dm<sup>-3</sup>.

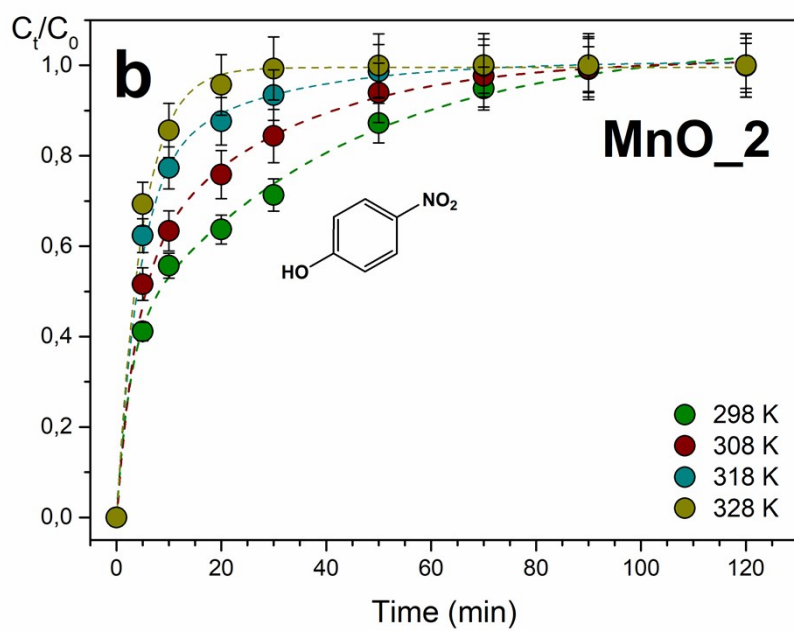
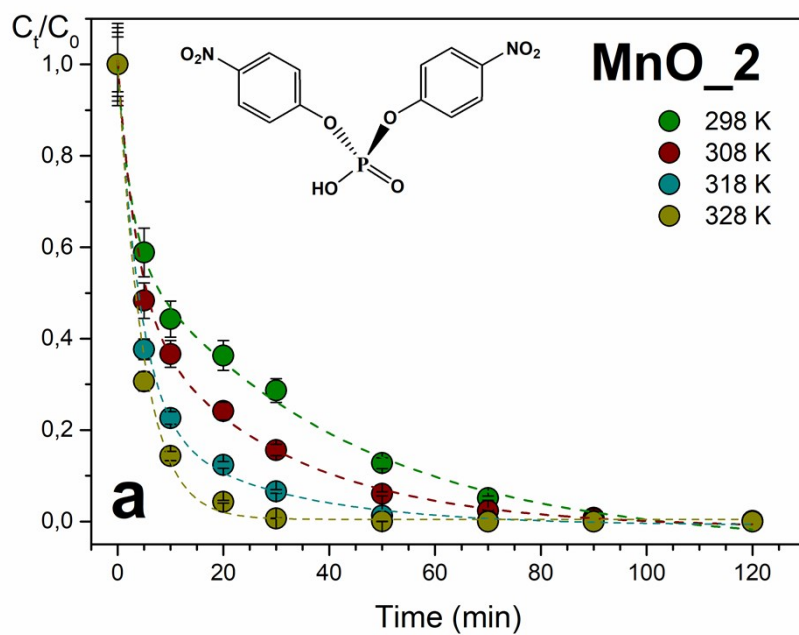


**Fig. S10.** Plots of pseudo-first-order kinetics of a) BNPP hydrolysis and b) 4-NP formation with 100 mg of MnO<sub>2</sub> catalyst at various temperatures. Reaction conditions: pH= 7.0, [BNPP]<sub>0</sub> = 50 mg·dm<sup>-3</sup>.

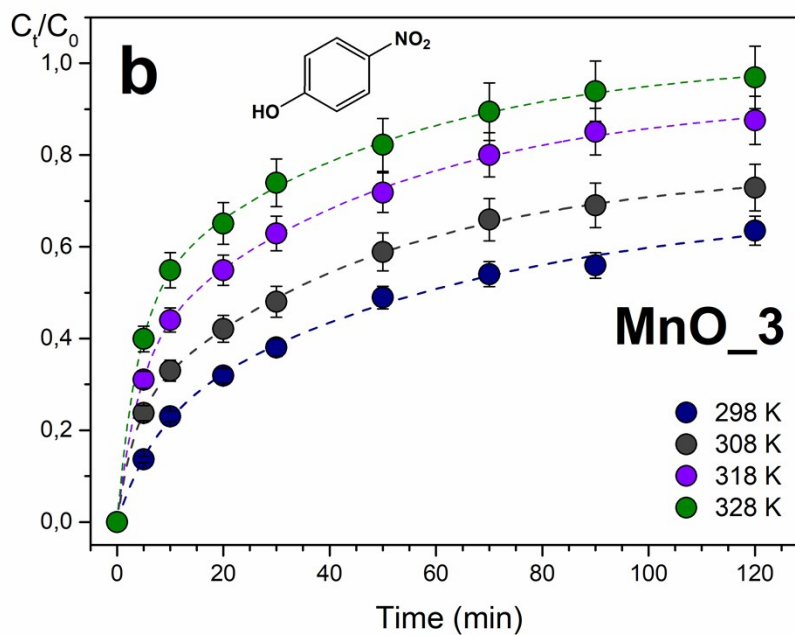
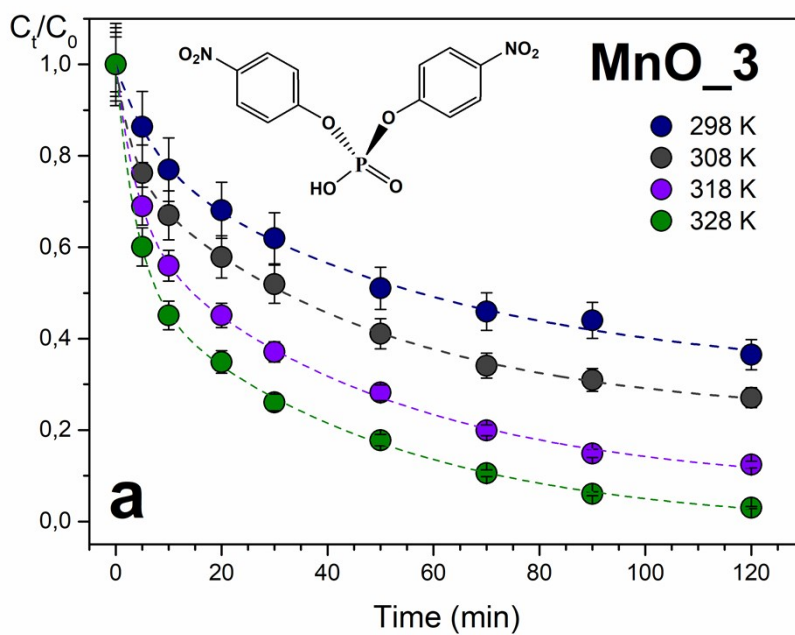


**Fig. S11.** Plots of pseudo-first-order kinetics of a) BNPP hydrolysis and b) 4-NP formation with 100 mg of MnO<sub>3</sub> catalyst at various temperatures. Reaction conditions: pH= 7.0, [BNPP]<sub>0</sub> = 50 mg·dm<sup>-3</sup>.

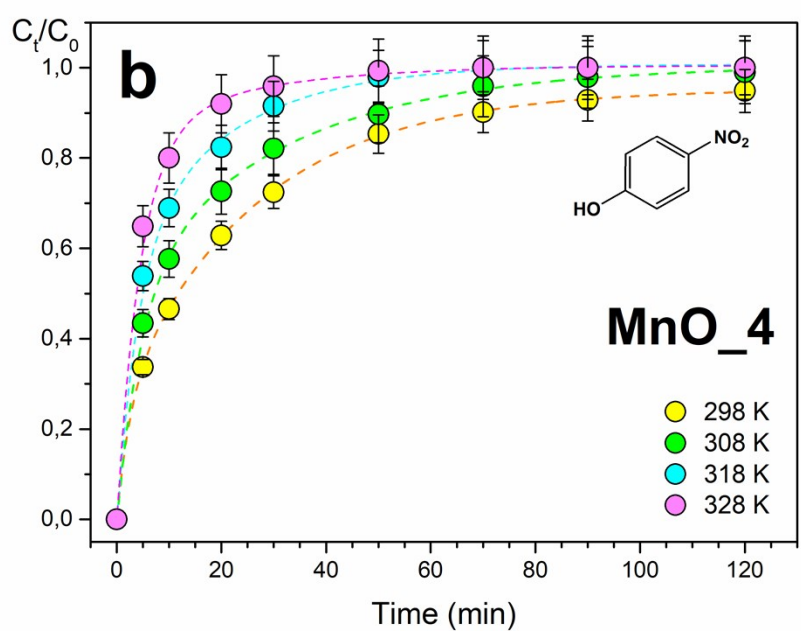
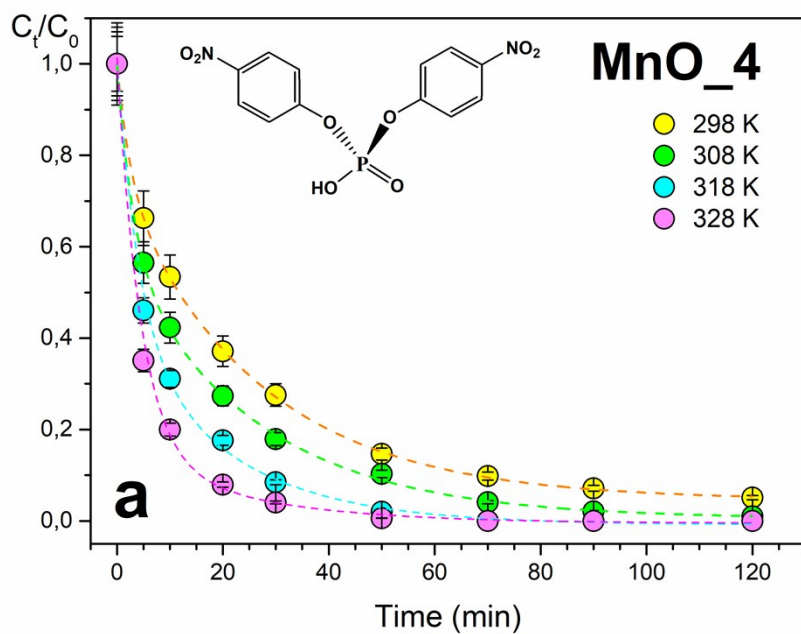


**Fig. S12.** Plots of pseudo-first-order kinetics of a) BNPP hydrolysis and b) 4-NP formation with 100 mg of MnO<sub>4</sub> catalyst at various temperatures. Reaction conditions: pH= 7.0, [BNPP]<sub>0</sub> = 50 mg·dm<sup>-3</sup>.

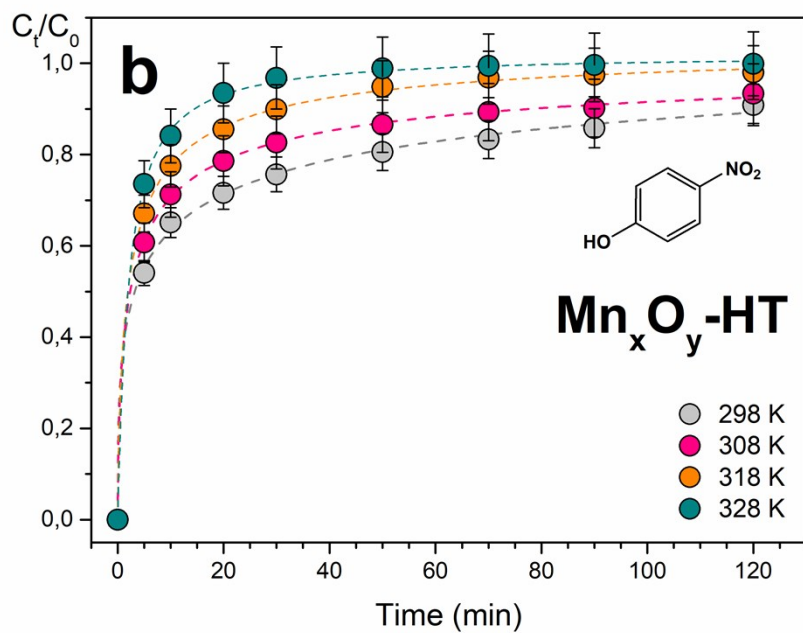
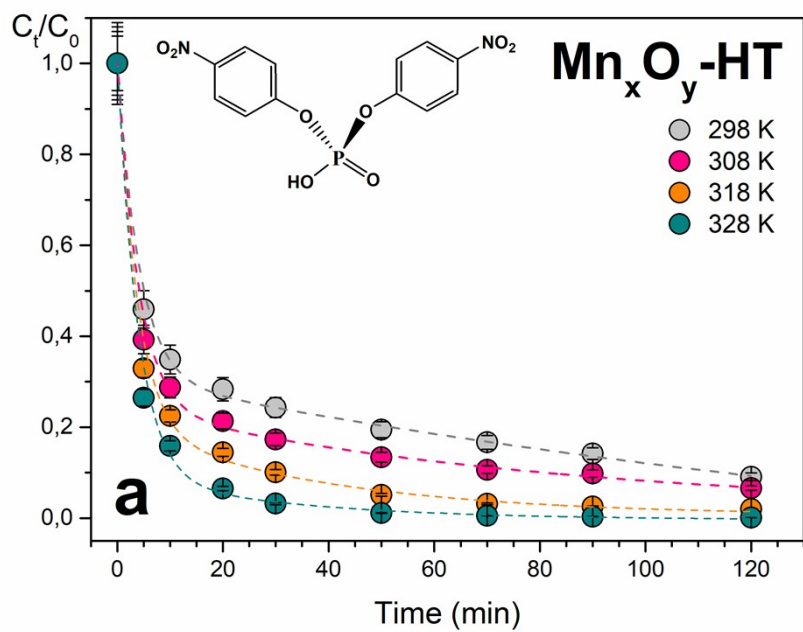


**Fig. S13.** Plots of pseudo-first-order kinetics of a) BNPP hydrolysis and b) 4-NP formation with 100 mg of  $Mn_xO_y-HT$  catalyst at various temperatures. Reaction conditions: pH= 7.0,  $[BNPP]_0 = 50 \text{ mg}\cdot\text{dm}^{-3}$ .

**Table S5.** Parameters of the pseudo-first-order kinetic model and  $E_a$  values for hydrolysis of BNPP at different temperatures on  $MnO_x$  prepared by the different synthesis methods (OriginPro 9.0).

Temperature (K)	$MnO_1^*$					
	$k_{BNPP} \pm SE^a$ ( $\text{min}^{-1}$ )	$d$ ( $\% \cdot 60 \text{ min}^{-1}$ ) <sup>b</sup>	$v_i$ ( $\mu\text{mol} \cdot \text{dm}^{-3} \cdot \text{min}^{-1} \cdot \text{g}^{-1}$ ) <sup>c</sup>	$\tau_{1/2}$ (min) <sup>d</sup>	$R^2$	$E_a$ ( $\text{kJ} \cdot \text{mol}^{-1}$ ) <sup>e</sup>
298	$0.038 \pm 0.004$	43.2	11.8	18.2	0.9973	34.5
308	$0.062 \pm 0.002$	63.2	17.4	11.2	0.9943	
318	$0.091 \pm 0.003$	74.4	23.2	7.6	0.9916	
328	$0.060 \pm 0.004$	81.4	13.9	11.6	0.9986	
$MnO_2^*$						
298	$0.083 \pm 0.001$	89.8	20.2	8.4	0.9985	25.1
308	$0.101 \pm 0.003$	95.7	25.3	6.9	0.9931	
318	$0.155 \pm 0.010$	98.5	30.6	4.5	0.9908	
328	$0.202 \pm 0.015$	99.6	34.0	3.4	0.9895	
$MnO_3^*$						
298	$0.023 \pm 0.002$	50.4	6.7	30.1	0.9951	34.2
308	$0.041 \pm 0.004$	62.2	11.6	16.9	0.9994	
318	$0.060 \pm 0.002$	76.7	15.2	11.6	0.9991	
328	$0.082 \pm 0.003$	86.9	19.6	8.5	0.9993	
$MnO_4^*$						
298	$0.063 \pm 0.001$	87.8	16.5	11.0	0.9998	23.4
308	$0.089 \pm 0.002$	93.4	21.3	7.8	0.9992	
318	$0.115 \pm 0.001$	98.2	26.4	6.0	0.9935	
328	$0.151 \pm 0.001$	99.6	31.8	4.6	0.9911	
$Mn_xO_y\text{-HT}^*$						
298	$0.159 \pm 0.038$	81.0	32.1	4.4	0.9892	10.9
308	$0.163 \pm 0.007$	86.9	34.5	4.2	0.9869	
318	$0.209 \pm 0.008$	94.8	37.4	3.3	0.9848	
328	$0.230 \pm 0.001$	98.8	41.5	3.0	0.9834	

[a]  $SE$  is the standard error of the estimated parameter [ $\text{min}^{-1}$ ]

[b]  $d$  is the degree of BNPP conversion after 60 min [ $\% \cdot 60 \text{ min}^{-1}$ ]

[c]  $v_i$  is the initial rate of conversion calculated according to equation No. 14 [ $\mu\text{mol}\cdot\text{dm}^{-3}\cdot\text{min}^{-1}\cdot\text{g}^{-1}$ ]

[d]  $\tau_{1/2}$  is the half-life of the reaction calculated from the rate constant according to equation No. 13 [min]

[e]  $E_a$  is the activation energy calculated from each observed rate constants at different temperature values according to equation No. 16 [ $\text{kJ}\cdot\text{mol}^{-1}$ ]

[\*] Reaction conditions: pH= 7.0,  $[\text{BNPP}]_0 = 50 \text{ mg}\cdot\text{dm}^{-3}$

**Table S6.** Parameters of the pseudo-first-order kinetic model for the formation of 4-NP on manganese catalysts prepared by the different synthesis methods (OriginPro 9.0).

Temperature (K)	<i>MnO_1*</i>			
	$k \pm \text{SEa}^1$ ( $\text{min}^{-1}$ )	$d$ (%) <sup>a)</sup>	$\tau_{1/2}$ (min)	$R^2$
298	$0.035 \pm 0.001$	42.1	19.8	0.9931
308	$0.059 \pm 0.004$	62.4	11.7	0.9928
318	$0.088 \pm 0.002$	73.5	7.9	0.9912
328	$0.057 \pm 0.001$	80.2	12.2	0.9986
<i>MnO_2*</i>				
298	$0.081 \pm 0.003$	90.1	8.6	0.9952
308	$0.099 \pm 0.005$	94.8	7.0	0.9983
318	$0.152 \pm 0.011$	97.8	4.6	0.9936
328	$0.197 \pm 0.013$	99.5	3.5	0.9742
<i>MnO_3*</i>				
298	$0.020 \pm 0.001$	50.0	34.7	0.9985
308	$0.043 \pm 0.002$	61.8	16.1	0.9980
318	$0.059 \pm 0.001$	76.5	11.7	0.9997
328	$0.080 \pm 0.002$	86.8	8.7	0.9985
<i>MnO_4*</i>				
298	$0.060 \pm 0.002$	87.5	11.6	0.9987
308	$0.090 \pm 0.001$	92.8	7.7	0.9974
318	$0.116 \pm 0.003$	98.1	6.0	0.9896
328	$0.155 \pm 0.001$	99.4	4.5	0.9976
<i>Mn<sub>x</sub>O<sub>y</sub>-HT*</i>				
298	$0.140 \pm 0.002$	83.1	4.9	0.9894

308	$0.155 \pm 0.001$	88.2	4.5	0.9877
318	$0.195 \pm 0.002$	95.5	3.5	0.9978
328	$0.222 \pm 0.009$	99.1	3.1	0.9889

[a]  $SE$  is the standard error of the estimated parameter [ $\text{min}^{-1}$ ]

[b]  $d$  is the degree of BNPP conversion after 60 min [ $\% \cdot 60 \text{ min}^{-1}$ ]

[c]  $\tau_{1/2}$  is the half-life of the reaction calculated from the rate constant according to equation No. 3 [min]

[\*] Reaction conditions:  $\text{pH}=7.0$ ,  $[\text{BNPP}]_0 = 50 \text{ mg} \cdot \text{dm}^{-3}$

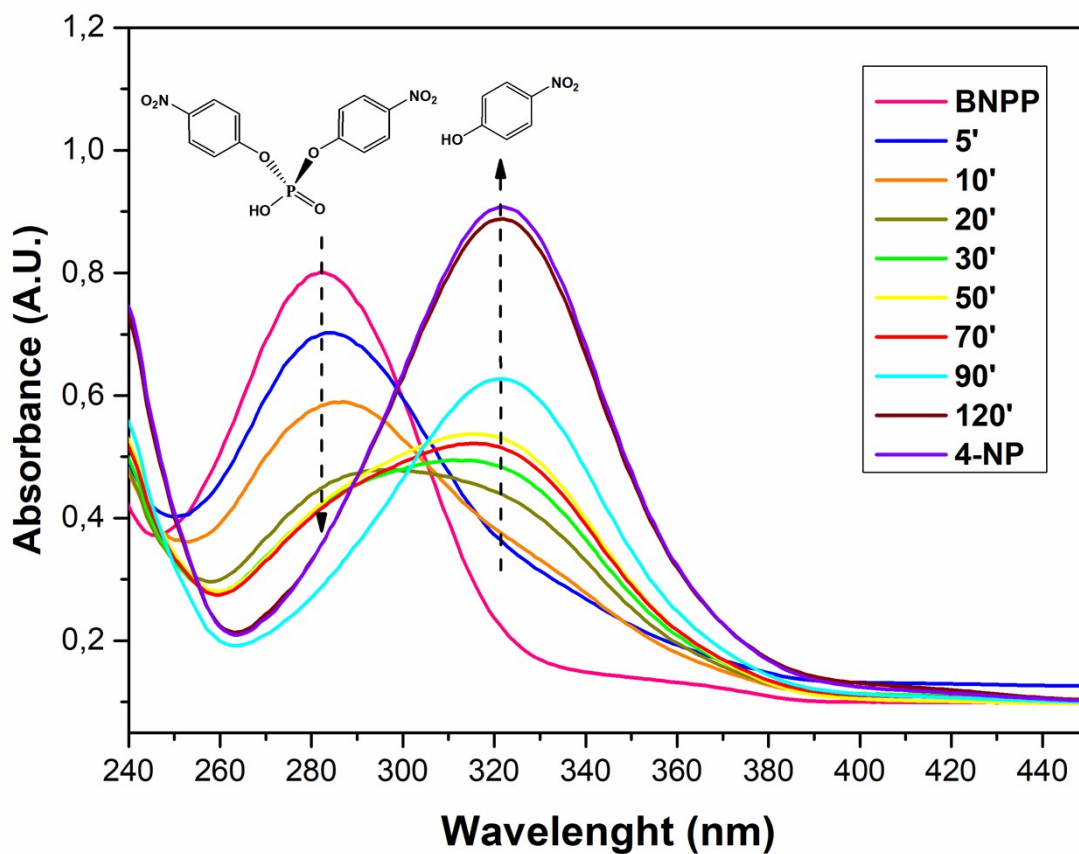


**Fig. S14.** An example of time-resolved UV-Vis spectra of collected supernatants during the BNPP catalytic hydrolysis.

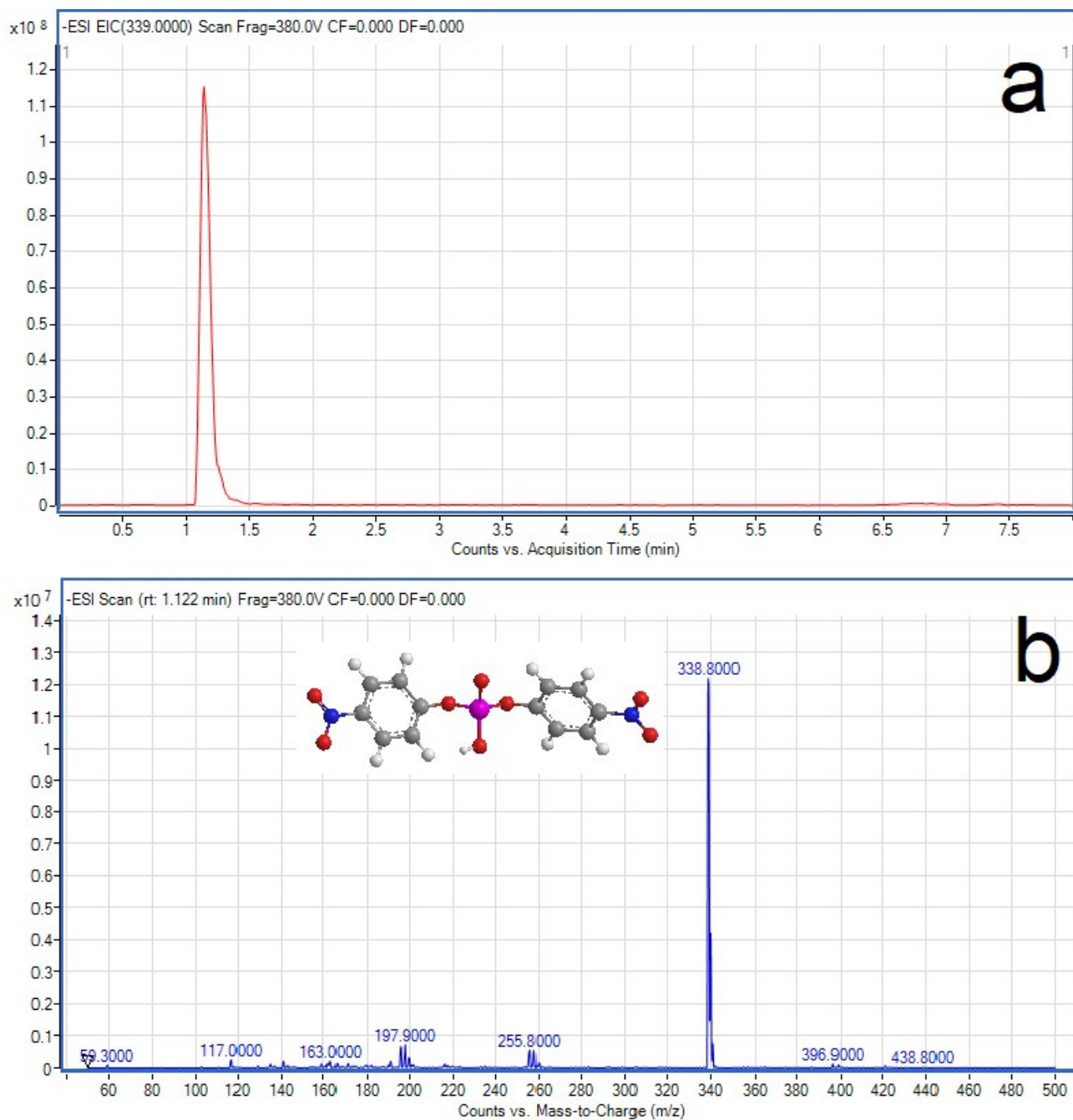


**Fig. S15.** Extracted ion chromatogram (a) and electrospray ionization mass spectra (b) of BNPP molecule.

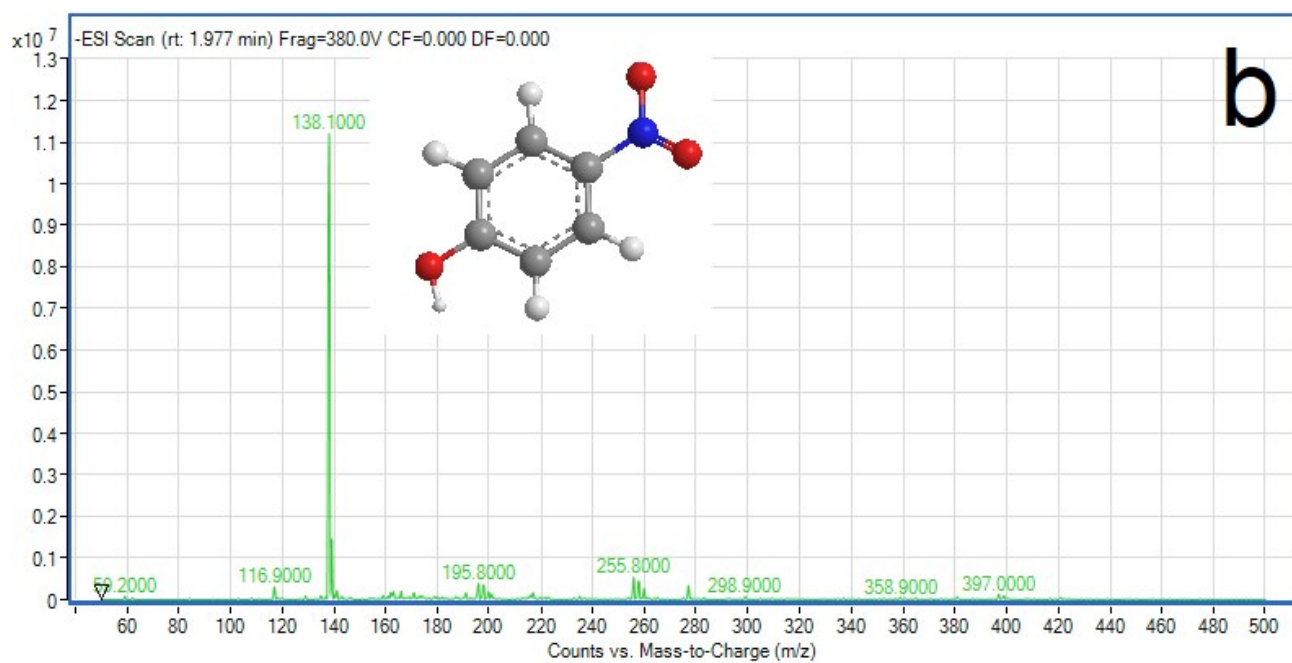
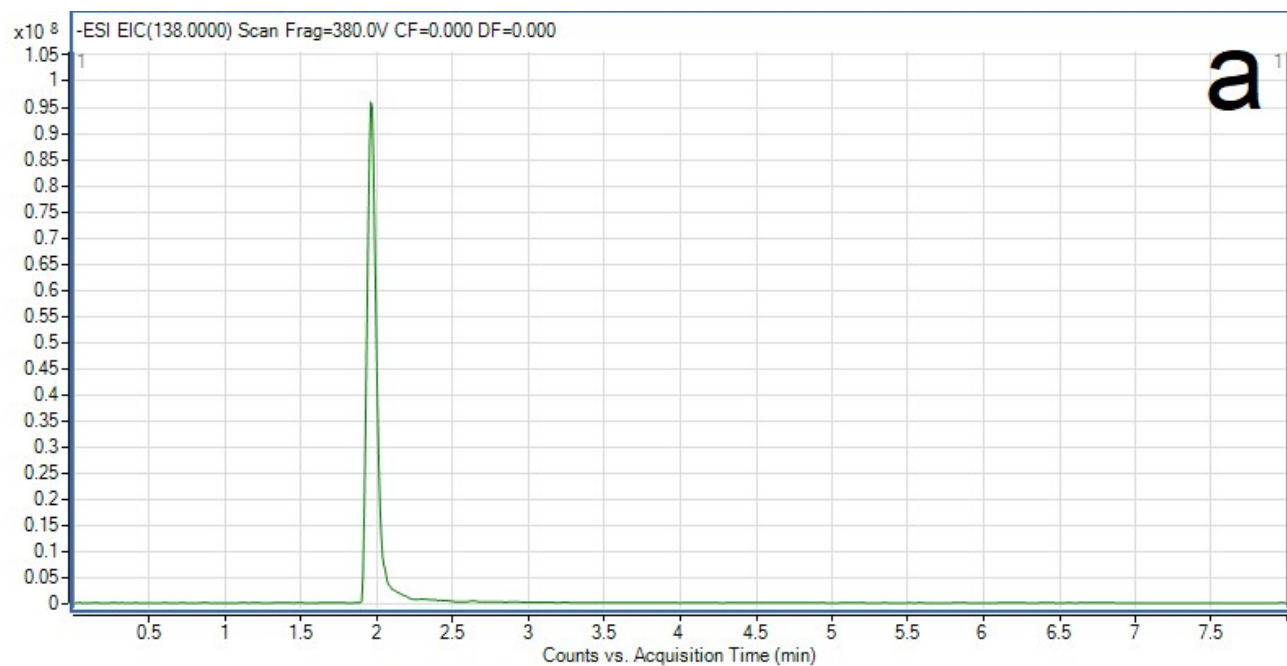


**Fig. S16.** Extracted ion chromatogram (a) and electrospray ionization mass spectra (b) of 4-NP molecule.

**Table S7.** Catalytic evaluation results for the MnO<sub>x</sub>-based catalysts: Temperature for 30% conversion (T<sub>30%</sub>) and specific activity SA (per unit BET, T=700 K).

Sample	T <sub>30%</sub> , K	SA, mol·m <sup>-2</sup>
MnO_1	663	1.52
MnO_2	719	0.25
MnO_3	681	0.86
MnO_4	633	3.79
Mn <sub>x</sub> O <sub>y</sub> -HT	684	6.89

**Table S8.** Temperature-dependent selectivity of individual by-products.

MnO_1 Selectivity, %				MnO_2 Selectivity, %				MnO_3 Selectivity, %				MnO_4 Selectivity, %				Mn <sub>x</sub> O <sub>y</sub> -HT Selectivity, %			
T, K	CO <sub>2</sub>	CH <sub>4</sub>	CO	T, K	CO <sub>2</sub>	CH <sub>4</sub>	CO	T, K	CO <sub>2</sub>	CH <sub>4</sub>	CO	T, K	CO <sub>2</sub>	CH <sub>4</sub>	CO	T, K	CO <sub>2</sub>	CH <sub>4</sub>	CO
637	8,9	2,7	88	640	38,2	3,7	58	670	9,7	7,3	81	678	7,0	7,1	84	674	0	13,0	87
663	7,2	7,1	82	664	10,8	7,7	81	681	8,5	9,0	80	697	7,4	7,3	84	684	0	10,8	89
695	6,4	8,6	83	694	24,5	27,3	41	706	7,6	9,2	81	716	7,6	8,0	83	719	0	11,6	88
721	6,3	6,8	87	719	10,9	13,2	75	724	8,3	9,9	80	725	8,6	8,1	82	731	0	12,6	87

**Table S9.** Yield table of the intermediates and by-products.

	T, K	CH <sub>4</sub> (% Yield)	CO <sub>2</sub> (% Yield)	CO (% Yield)	C <sub>3</sub> -C <sub>4</sub> (% Yield)	MF (% Yield)
<b>MnO_1</b>	749	8.5	6.0	73.4	0	2.0
<b>MnO_2</b>	759	5.0	5.7	59.4	0	2.0
<b>MnO_3</b>	724	5.7	4.8	45.3	0	2.0
<b>MnO_4</b>	725	7.9	8.3	78.8	2.0	0
<b>Mn<sub>x</sub>O<sub>y</sub>-HT</b>	731	10.7	0	73.7	0	0

**Table S10.** Summary of methanol conversion, by-products selectivities, and carbon balance calculated for 660 and 720K temperatures.

	<b>MnO_1</b>		<b>MnO_2</b>		<b>MnO_3</b>		<b>MnO_4</b>		<b>Mn<sub>x</sub>O<sub>y</sub>-HT</b>	
	660K	720K	660K	720K	660K	720K	660K	720K	660K	720K
Methanol conversion, %	32	84	20	31		57	56	96		75
Carbon balance, %	100	100	100	100	100	100	100	100	100	100
CO <sub>2</sub> selectivity, %	7.2	6.2	10.8	10.9	9.7	8.3	7.2	7.6	0	0
CO selectivity, %	82	87	81	75	81	80	85	83	87	87
CH <sub>4</sub> selectivity, %	7.1	6.8	7.7	13.2	7.3	9.9	6.1	8	13	12.6
Methyl formate, %	2.7	0	0.5	0.9	2	1.8	0	0	0	0.4
C <sub>2</sub> -C <sub>3</sub> selectivity, %	1	0	0	0	0	0	1.7	1.4	0	0

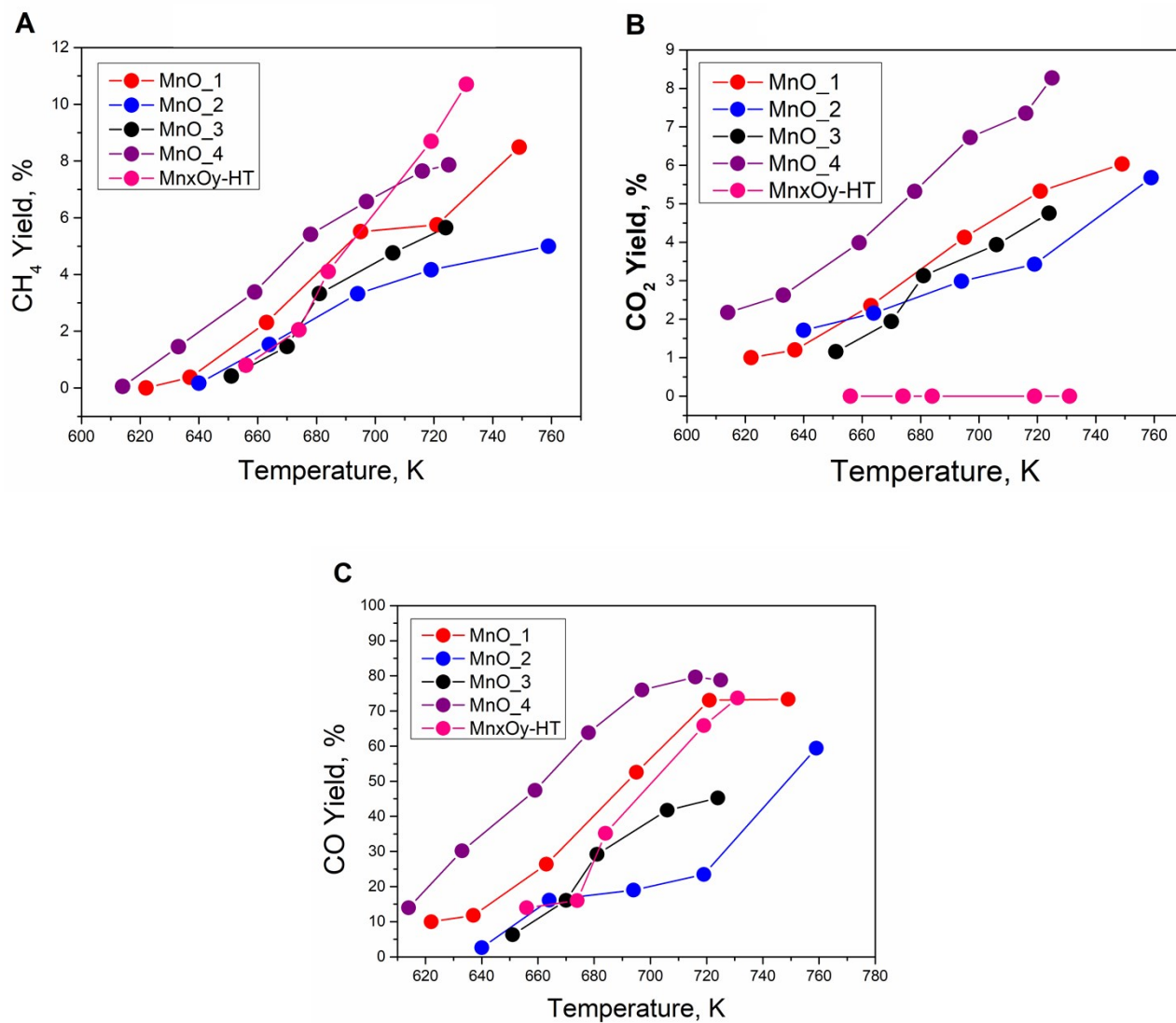


**Fig. S17.** Temperature-dependent yield (%) of the by-products: Methane (A), Carbon dioxide (B), and Carbon monoxide (C).

## References

- 1 S. Gražulis, A. Merkys and A. Vaitkus, in *Handbook of Materials Modeling*, 2018.
- 2 K. Momma and F. Izumi, *J. Appl. Crystallogr.*, DOI:10.1107/S0021889811038970.
- 3 a. L. Patterson, *Phys. Rev.*, 1939, **56**, 978–982.
- 4 M. Naderi, in *Progress in Filtration and Separation*, 2014, pp. 585–608.
- 5 E. Moazzen, E. V. Timofeeva and C. U. Segre, *J. Mater. Sci.*, , DOI:10.1007/s10853-017-1018-5.
- 6 G. Qiu, J. Wang, W. Zhao, X. Feng, W. Tan, Q. Zhang and F. Liu, *Chinese J. Chem.*, DOI:10.1002/cjoc.201090380.
- 7 M. Lin, B. Chen, X. Wu, J. Qian, L. Fei, W. Lu, L. W. H. Chan and J. Yuan, *Nanoscale*, DOI:10.1039/c5nr07900d.
- 8 X. Wang, G. Lv, L. Liao and G. Wang, *RSC Adv.*, DOI:10.1039/c5ra08486e.
- 9 M. H. Rossouw, A. De Kock, D. C. Liles, R. J. Gummow and M. M. Thackeray, *J. Mater. Chem.*, , DOI:10.1039/jm9920201211.
- 10 S. Ching, J. L. Roark, N. Duan and S. L. Suib, *Chem. Mater.*, DOI:10.1021/cm960460k.
- 11 K. S. Abou-El-Sherbini, M. H. Askar and R. Schöllhorn, *Solid State Ionics*, , DOI:10.1016/S0167-2738(02)00258-8.
- 12 D. Jarosch, *Mineral. Petrol.*, , DOI:10.1007/BF01163155.
- 13 C. Julien and M. Massot, *Phys. Chem. Chem. Phys.*, , DOI:10.1039/b203361e.
- 14 C. Revathi and R. T. R. Kumar, *Electroanalysis*, DOI:10.1002/elan.201600608.
- 15 T. Gao, M. Glerup, F. Krumeich, R. Nesper, H. Fjellvåg and P. Norby, *J. Phys. Chem. C*, , DOI:10.1021/jp804924f.
- 16 T. Gao, H. Fjellvåg and P. Norby, *Anal. Chim. Acta*, , DOI:10.1016/j.aca.2009.06.059.
- 17 Y. Dong, K. Li, P. Jiang, G. Wang, H. Miao, J. Zhang and C. Zhang, *RSC Adv.*, DOI:10.1039/c4ra02654c.
- 18 P. Yang, S. Lee, J. E. Post, H. Xu, Q. Wang, W. Xu and M. Zhu, *Geochim. Cosmochim. Acta*, , DOI:10.1016/j.gca.2018.08.014.
- 19 W. Zhao, F. Liu, X. Feng, W. Tan, G. Qiu and X. Chen, *Clay Miner.*, DOI:10.1180/claymin.2012.047.2.04.
- 20 D. Lan, M. Qin, R. Yang, H. Wu, Z. Jia, K. Kou, G. Wu, Y. Fan, Q. Fu and F. Zhang, *J. Mater. Sci. Mater. Electron.*, , DOI:10.1007/s10854-019-01201-7.
- 21 H. Y. Xu, S. Le Xu, H. Wang and H. Yan, *J. Electrochem. Soc.*, DOI:10.1149/1.2098267.
- 22 T. Gao, P. Norby, F. Krumeich, H. Okamoto, R. Nesper and H. Fjellvåg, *J. Phys. Chem. C*, ,

DOI:10.1021/jp9097606.

- 23 J. Du, Y. Gao, L. Chai, G. Zou, Y. Li and Y. Qian, *Nanotechnology*, DOI:10.1088/0957-4484/17/19/024.
- 24 Q. Javed, F. P. Wang, M. Y. Rafique, A. M. Toufiq, Q. S. Li, H. Mahmood and W. Khan, *Nanotechnology*, , DOI:10.1088/0957-4484/23/41/415603.
- 25 E. R. Stobbe, B. A. De Boer and J. W. Geus, *Catal. Today*, , DOI:10.1016/S0920-5861(98)00296-X.
- 26 F. E. Sesen, *J. Chem. Technol. Appl.*, DOI:10.35841/chemical-technology.1.1.26-27.
- 27 K. T. Jacob, A. Kumar, G. Rajitha and Y. Waseda, *High Temp. Mater. Process.* 30, pp. 459-472.
- 28 F. Chen, S. Zhao, T. Yang, T. Jiang, J. Ni, H. Xiong, Q. Zhang and X. Li, *Chinese J. Chem. Eng.*, , DOI:10.1016/j.cjche.2019.01.038.
- 29 F. Kapteijn, L. Singoredjo, A. Andreini and J. A. Moulijn, *Appl. Catal. B, Environ.*, , DOI:10.1016/0926-3373(93)E0034-9.
- 30 M. H. Castaño, R. Molina and S. Moreno, *Mol. Catal.*, , DOI:10.1016/j.mcat.2017.09.015.
- 31 D. S. Lee, T. H. Kim, C. H. Park, C. Y. Chung, Y. S. Lim, W. S. Seo and H. H. Park, *CrystEngComm*, DOI:10.1039/c3ce40643a.